

1 **The interseismic velocity field of the Central Apennine from a dense GPS**
2 **network**

3

4 **Galvani A.¹, Anzidei M.¹, Devoti R.¹, Esposito A.¹, Pietrantonio G.¹, Pisani A. R.¹,**
5 **Riguzzi F.¹, Serpelloni E.²**

6

7 ¹ Istituto Nazionale di Geofisica e Vulcanologia, Centro Nazionale Terremoti, Via di Vigna
8 Murata, 605 – 00143 Rome, Italy – www.ingv.it

9 ² Istituto Nazionale di Geofisica e Vulcanologia, Centro Nazionale Terremoti, Via Donato
10 Creti, 12 - 40128 Bologna, Italy – www.bo.ingv.it

11

12 Alessandro Galvani – Istituto Nazionale di Geofisica e Vulcanologia, Centro Nazionale
13 Terremoti, Via di Vigna Murata, 605 – Rome, Italy – www.ingv.it

14 +39-06-51860225

15 alessandro.galvani@ingv.it

16 **Abstract**

17 Since 1999 we have repeatedly surveyed the Central Apennines by a dense survey style
18 geodetic network, the Central Apennine Geodetic Network (CAGeoNet), consisting of 123
19 benchmarks distributed over an area of $\sim 180 \times 130$ km extend, from the Tyrrhenian to the
20 Adriatic coasts with an average inter-site distance of 3-5 km. The network is located across
21 the main seismogenic structures of the region, capable to generate destructive earthquakes.
22 Here, we show the horizontal GPS velocity field of both the CAGeoNet and continuous
23 GPS (CGPS) stations in this region, estimated from the position time series in the time span
24 1999-2007. We have analyzed the data using both the Bernese and the Gamit software,
25 rigorously combining the two solutions to obtain a validated result. Then, we have analyzed
26 the strain rate field, which shows a region of extension located along the axis of the
27 Apennines chain, with values ranging from 2 to $66 \cdot 10^{-9}$ yr⁻¹ and a relative minimum of
28 about $20 \cdot 10^{-9}$ yr⁻¹ located in the L'Aquila basin area. Our velocity field represents an
29 improved estimation of the ongoing elastic inter-seismic deformation of central Apennines
30 in particular of the L'Aquila earthquake of April 6th, 2009 area.

31

32 **Key words:** Central Apennines, GPS velocity field, solutions combination, GPS surveys

33 **Introduction**

34 According to current views, the Apennines chain is an arc-shaped, NE verging belt,
35 characterized by a complex pattern of thrust and folds and normal faults related to two
36 superimposed tectonic phases: an upper Miocene - lower Pleistocene compressional phase,
37 forming NW–SE trending thrust and folds, and the subsequent Quaternary extensional
38 phase, forming NW–SE trending normal faults responsible for the formation of large
39 intramontane basins, filled by Plio–Quaternary continental sediments (i.e. L’Aquila, Rieti,
40 Terni, Fucino and Sulmona basins) (Galadini & Messina, 1994; Galadini & Galli, 2000)
41 (Fig. 1). Some authors explain the change of the tectonic regime as caused by the flexural
42 retreat, through a roll back mechanism, of the lithospheric Adriatic plate dipping below the
43 Apennines (Reutter et al., 1980; Boccaletti et al., 1982; Malinverno and Ryan, 1986;
44 Royden et al., 1987; Patacca et al., 1990; Doglioni, 1991; Doglioni et al., 1994; Frepoli e
45 Amato 1997; Basili & Barba, 2007). Other authors ascribe the change of the tectonic
46 regime as caused by the NE motion, relative to Eurasia, of the Adriatic microplate around a
47 rotation pole located in NW Italy (Anderson & Jackson, 1987; Calais et al., 2002;
48 D’Agostino et al., 2005; D’Agostino et al., 2008). At present, geodetic data show that
49 extensional deformation in the central Apennines is occurring along a narrow belt 30–40
50 km wide (Hunstad et al., 2003; Serpelloni et al., 2005; Devoti et al., 2008; Devoti et al.,
51 2011), near the areas where the strongest historical (intensity \geq XI) and instrumental
52 earthquakes occurred (Boschi et al., 1998; Selvaggi, 1998) (Fig.1). Starting from 1999 a
53 dense survey-mode GPS network (CAGeoNet) consisting of 123 benchmarks with an
54 average inter-site distance of 3-5 km, now surrounded by continuously operating GPS
55 stations (Fig.2), was designed and installed in the central Apennines (Anzidei et al., 2005;
56 Anzidei et al., 2008) across the main active faults, as evidenced by geological and
57 seismological data (Valensise & Pantosti, 2001; Galadini & Galli, 2000). The high GPS
58 stations density and the quality of the data collected, provide new insights about the
59 present-day deformation of this seismically active area, and gives information useful for
60 seismic hazard assessments.

61 It has been shown that the combination of independent geodetic solutions, obtained with
62 different GPS-processing software (Avallone et al., 2010; Devoti et al., 2012) allows to
63 minimize eventual systematic errors and to validate the final velocity solutions. In this

64 work, we estimate the interseismic strain-rates from the combination of independent
65 solutions obtained with the Bernese and Gamit softwares, thus investigating the geodetic
66 deformation of the interseismic cycle of the Umbria-Marche Apennines (UMA) and Lazio–
67 Abruzzo Apennines (LAA).

68

69 **The CAGeoNet and GPS campaigns**

70 The CAGeoNet network has been repeatedly measured during the time span 1999-2007.
71 Surveys were planned taking into account the network grid, the number of stations to be
72 measured simultaneously (up to 11) and the time required to move receivers through the
73 network. Consistently with the logistics, measurements have been carried out
74 approximately in the same period of the year to minimize possible biases due to seasonal
75 variations. Each station was occupied for an average observation window of 48 h, for at
76 least three survey sessions per station, with a sampling rate of 30 s.

77 Here we discuss the interseismic deformation field resulting from the analysis of velocities
78 obtained from a sub-set of 55 CaGeoNet stations in the time-interval 1999-2007.

79

80 **Data processing and combination procedure**

81 The analyzed data set (Fig. 2) consists of GPS data collected on survey style benchmarks
82 (the CAGeoNet benchmarks) and continuous data provided by the CGPS networks located
83 in the Central Apennine region. The CGPS stations belonging to different GPS networks:
84 IGS (<http://igsceb.jpl.nasa.gov>), RING (Avallone et al., 2010), ASI (Vespe et al., 2000),
85 Leica Geosystems (ItalPos network), the Regione Abruzzo and the Universities of Perugia
86 and L'Aquila.

87 The GPS data cover the period from 1999 to 2007, and are arranged into several clusters,
88 each one sharing common fiducial CGPS stations used as anchor stations in the subsequent
89 combination. Each cluster has been independently processed, then combined by a least
90 squares combination into a single daily solution. The GPS observations have been
91 processed using both the Bernese 5.0 (Beutler et al., 2007) and Gamit 10.34 software
92 (Herring et al., 2006).

93 The BERNESE processing is based on the BPE procedure, following the standard analysis
94 for regional networks. We solve for daily stations coordinates together with hourly

95 troposphere parameters, using the a priori DRY NIELL troposphere model and estimating
96 the corrections by the WET NIELL mapping function. Ionosphere was neither estimated
97 nor modelled since we used the L3 (ionosphere-free) linear combination of L1 and L2. The
98 a priori GPS orbits and Earth Orientation Parameters were fixed to the precise IGS
99 products. We applied the ocean-loading model FES2004 and used the International GNSS
100 Service (IGS) absolute antenna phase-center corrections. The daily solutions were obtained
101 in a loosely constrained reference frame, i.e. all the a priori stations coordinates were left
102 free to 10 m apriori sigma.

103 The GAMIT processing follows the standard procedures for the analysis of regional
104 networks (e.g., McClusky et al., 2000; Serpelloni et al., 2006), applying loose constraints
105 to the geodetic parameters. The GAMIT software uses double-differenced, ionosphere-free
106 linear combinations of the L1 and L2 phase observations, to generate weighted least square
107 solutions for each daily session (Schaffrin & Bock, 1988; Dong & Bock, 1989). An
108 automatic cleaning algorithm (Herring et al., 2006) is applied to post-fit residuals, in order
109 to repair cycle slips and to remove outliers. The observation weights vary with elevation
110 angle and are derived individually for each station from the scatter of post-fit residuals
111 obtained in a preliminary GAMIT solution. The effect of solid-earth tides, polar motion and
112 oceanic loading are taken into account according to the IERS/IGS standard 2003 model
113 (McCarthy and Petit, 2004). We apply the ocean-loading model FES2004 and use the IGS
114 absolute antenna phase-center correction table to model the effective receiver and satellites
115 antennas phase-centers. We use orbits provided by the Scrips Orbit Permanent Array
116 Center (SOPAC). Estimated parameters for each daily solution include the 3D cartesian
117 coordinates for each station, the 6 orbital elements for each satellite, Earth Orientation
118 Parameters (pole position and rate and UT1 rate) and integer phase ambiguities, applying
119 loosely constraints (~10 m) to the apriori parameters. We also estimate hourly piecewise-
120 linear atmospheric zenith delays at each station to correct the poorly modelled troposphere,
121 and 3 east-west and north-south atmospheric gradients per day, to account for azimuth
122 asymmetry; the associated error covariance matrix is also computed and saved in SINEX
123 format.

124 Both the analysis procedures (BERNESE and GAMIT) produce daily loosely constrained
125 solutions, i.e. free from any a priori reference frame datum. Coordinates and the complete
126 associated covariance matrices were saved in SINEX format.

127 The time series of the two solutions were then obtained applying minimal inner constraints
128 and a 4-parameter Helmert transformation to obtain coordinates and errors expressed in the
129 IGS05 reference frame (the IGS realization of the ITRF2005 reference frame). Then, we
130 obtained a velocity field for each solution estimating a linear drift (velocity), annual
131 sinusoid and occasional offsets due to changes in the stations equipment from each time
132 series.

133

134 **Combined GPS velocity field**

135 The two independent velocity solutions were combined in a unique velocity solution using
136 a linear least squares combination approach. The normal matrix is formed from the two
137 independent velocity solutions and then inverted to estimate the unified velocity field of the
138 entire network. Since usually the covariance matrix is known apart from a constant
139 multiplier, we estimate also a solution scale factor together with the combined velocity
140 solution. This ensures that the individual χ^2 of each velocity solution are equally balanced
141 (individual solutions do not prevail in the combination process) and the total χ^2 is close to
142 unity (realistic errors). The combined solution represents a weighted velocity average
143 taking into account the correlation matrices of the two solutions. The differences between
144 the combined and the individual solutions have low mean values and comparable standard
145 deviations (Fig. 3). The values reported in Figure 3 show how the combined solution is
146 placed between the BERNESE and GAMIT solutions and does not give priority to any
147 individual solution. The BERNESE solution is slightly more noisy in the east velocity
148 component while the GAMIT solution is slightly more noisy in the north velocity
149 component. The comparison between BERNESE and GAMIT solutions shows residuals
150 whose average are -0.2 mm yr^{-1} (Ve component) and 0.3 mm yr^{-1} (Vn component) and
151 dispersion values (at 1σ level) of 0.7 mm yr^{-1} and 0.9 mm yr^{-1} in Ve and Vn, respectively.
152 The differences are comparable with the averaged sigma values computed for the
153 permanent stations used in the individual solutions ($\sigma_E = 0.14 \text{ mm}$; $\sigma_N = 0.23 \text{ mm}$),
154 highlighting how the solutions are compatible. We have made a statistical screening

155 between the combined solution with respect to each single solution (BERNESE and
156 GAMIT) and the single solutions with respect to each other, both on permanent and non-
157 permanent stations, comparing the differences obtained between the average values of V_e
158 and V_n . Stations exhibiting differences greater than the respective 2σ values were
159 discarded.

160 The combined velocity field with respect to an Eurasian-fixed reference frame is shown in
161 Figure 4. The velocity components and their uncertainties are reported in Table 1. The
162 Eurasia plate has been fixed minimizing the horizontal velocities of 24 stations located in
163 the stable part of the plate. The selection of Eurasian stations is statistically inferred using a
164 χ^2 test-statistic to select the subset of stations defining the stable plate (Noquet et al., 2001)
165 starting from the triad WSTR, WTZR and ZIMM stations in ITRF2005. The estimated
166 Euler pole and rotation rate for Eurasia plate are at 55.85°N , 95.72°W and $0.266^\circ \pm 0.003^\circ$
167 Myr^{-1} respectively.

168 The geodetic strain rate has been evaluated by a distance-weighted approach, computed
169 using all stations on a regularly spaced grid applying the weighting algorithm developed by
170 Shen et al. (1996). The contribution of each station velocity to the strain-rate computed on a
171 given node, is down weighted with the function $W = \exp(-d^2/\alpha^2)$, where d is the distance
172 between each node and the stations and α is the smoothing distance parameter. The
173 algorithm selects the optimal α -value from a given *a priori* interval, depending on the
174 spatial distribution of the GPS sites, consequently strain-rate maps are obtained with
175 spatially variable α .

176 The second invariant rate has been obtained by interpolating the velocity horizontal
177 components on a $0.1^\circ \times 0.1^\circ$ regular grid. The smoothing factor down-weights the velocities
178 in the range from 20 to 100 km, according to the network density (Fig. 6).

179

180 **Results**

181 The combined horizontal velocity field, expressed with respect to a fixed Eurasian plate,
182 (Fig. 4) shows i) a good coherence between velocities estimated from CAGeoNet (red
183 arrows) and CGPS stations (blue arrows), ii) two different and characteristic main velocity
184 patterns; a NNW oriented trend on the Apennine-Tyrrhenian sector and a NNE oriented
185 trend on the Apennine-Adriatic sector. A gradual clockwise velocity rotation is clearly

186 evident from W to E, where velocities are initially NNW oriented and rotate towards NNE
187 increasing their values (0.9–5.2 mm yr⁻¹). This pattern shows an anomaly in the L'Aquila
188 basin where the vectors are turned ~ NS directed, normal to the main tectonic structures of
189 Gran Sasso Range (Fig. 4).

190 To better evidence the velocity gradients across the central Apennines chain, we have
191 represented the velocity field with respect to a fixed Tyrrhenian coast (Fig. 5) and then
192 projected the velocities along two profiles ENE – WSW oriented, crossing the studied area.

193 The two profiles are parallel to the average direction of the velocity vectors and
194 approximately normal to the main fault systems. Profile 1) is located across the Umbria-
195 Marche Apennines sector (UMA), profile 2) is located across the Lazio–Abruzzi Apennines
196 (LAA) sector. The projections contain all the velocities within the distance of 40 km
197 (profiles 1), and 30 km (profile 2). To highlight the velocity gradient, we use a moving-
198 average filter, with a 40 km window (grey line in Fig. 5). The net extension rates across the
199 two cross sections are the same, ~2.5 mm yr⁻¹, but spreading over different distances.
200 Profile 1 shows a velocity variation concentrated in a narrow strip of ~ 60 km, with
201 maximum step of 1.5 mm yr⁻¹ occurring in about 30 Km, on the western flank of the chain
202 with a strain rate of about $50 \cdot 10^{-9}$ yr⁻¹. Profile 2 shows a more irregular velocity variation,
203 with a negative (i.e., shortening component) gradient roughly in correspondence of
204 L'Aquila basin (between 120 and 150 km, Figure 5, profile 2), and developing along larger
205 distance (~ 100 km.) with respect to profile 1 with a lower strain rate of about $20 \cdot 10^{-9}$ yr⁻¹.

206 The predominantly extensional deformation is mainly oriented NE–SW, ranging from $2 \pm$
207 $11 \cdot 10^{-9}$ yr⁻¹ to $66 \pm 19 \cdot 10^{-9}$ yr⁻¹ (Fig. 6).

208 In Umbria-Marche Apennines (UMA) the extensional deformation is distributed in a
209 relatively wide area, coinciding with the culmination of topographic relief. The distribution
210 of extension area becomes to be narrower and shifted toward SW, crossing the Ancona-
211 Anzio Line (AAL), with slightly lower extension rates.

212 These estimations are in general agreement with those obtained by previous geodetic and
213 geologic data for this area. From geologic data, which include both interseismic and
214 coseismic deformations, Galadini & Galli (2000) obtain, across the main active fault sets
215 recognized in the area, an extension rate from 0.7 to 1.6 mm yr⁻¹; Faure Walker et. al (2010)
216 using fault slip vectors, calculate strain rates, averaged over 15 kyrs, of $12 \cdot 10^{-9}$ yr⁻¹ and an

217 extension rate of 1 mm yr^{-1} over a $160\times 80\text{ km}$ area, consistent with a strain rate $\leq 38\cdot 10^{-9}\text{ yr}^{-1}$
218 estimated in $5\times 80\text{ km}$ boxes crossing the strike of the central Apennines. From geodetic
219 data, Serpelloni et al. (2005) indicate $31\cdot 10^{-9}\text{ yr}^{-1}$, while D'Agostino et al (2008) show a
220 second invariant band parallel to the chain, with values $> 50\cdot 10^{-9}\text{ yr}^{-1}$. Devoti et al. (2008,
221 2011) estimate extension rate of $50\cdot 10^{-9}\text{ yr}^{-1}$. Our results disagree with those obtained by
222 Pesci et al. (2010), on a CAGeoNet network sub-set. They found a NE shortening in
223 correspondence of the Umbria-Marche Apennines, a NW shortening in the Liri Valley and
224 a wide area characterized by NE extension in the eastern portion of the Lazio–Abruzzo
225 Apennines.

226 A relative minimum of the strain second invariant ($20\pm 11\cdot 10^{-9}\text{ yr}^{-1}$) is evidenced in the
227 area where the April 6th, 2009 earthquake occurred (Fig. 6). This value is congruent, with
228 the extension rate of $10\pm 4\cdot 10^{-9}\text{ yr}^{-1}$ obtained by Doglioni et al (2011) using only CGPS
229 stations. The L'Aquila basin area, that experienced in the past large historical earthquakes,
230 has been characterized by a relative low instrumental seismicity in the last 30 years (1978 –
231 2008) (Fig. 1).

232 Viscoelastic earthquake cycle models (e.g., Lundgren et al. 2009) show that velocity
233 gradients across faults may depend on crustal rheology and the fault stage in the earthquake
234 cycle. The relative low strain-rate value observed across the L'Aquila basin by the dense
235 CaGeoNet network, could be interpreted, in this light, as due to its position in a later stage
236 of the earthquake cycle (e.g., Doglioni et al., 2011).

237

238 **Conclusion**

239 We processed more than 100 GPS stations in central Italy, combining both permanent and
240 survey-style networks. Thanks to the high number of stations and their short inter-distances
241 (3–5 km), our data set provides the most detailed view of the sub-regional deformation field
242 of this area. To validate our results, we have used two different strategies and GPS data
243 processing software. The two independent velocity solutions strongly agree (horizontal
244 WRMS 1.1 mm yr^{-1}) and their combination represents the best compromise of the available
245 solution. Since relevant seismicity did not occur in the Lazio-Abruzzo Apennine during the
246 considered time span (Fig. 1), we can assume that the observed velocity field is purely
247 inter-seismic, thus describing the regional and elastic deformation field before the 2008–

248 2009 L'Aquila seismic sequence, culminated with the April 6th 2009 M_w 6 earthquake. The
249 horizontal velocities of our non-permanent stations often show large uncertainties (average
250 values of about 1 and 1.5 mm yr⁻¹ in V_e , V_n respectively), nevertheless they are consistent
251 with the CGPS velocity field estimated in this area.

252 The horizontal velocities and the strain rate results are consistent with the major tectonic
253 features of the central Apennines showing a NE-SW extensional deformation style.

254 We estimate a differential velocity of about 2.5 mm yr⁻¹ across the Apennines, recognizing
255 two different extensional deformation patterns; the Umbria–Marche Apennines sector
256 shows a gradual velocity increase from W to E, while the Lazio–Abruzzo Apennines sector
257 shows an irregular velocity increase characterized by two small steps. A moderate velocity
258 decreasing is located in correspondence of the L'Aquila basin. The total strain rate values
259 range from 2 to $66 \cdot 10^{-9}$ yr⁻¹. A relative minimum of about $20 \cdot 10^{-9}$ yr⁻¹ is located in the area
260 of the L'Aquila basin, thus emphasizing the possible role of strain rate pattern in seismic
261 hazard assessment. Shen et al. 2007 observed that, regions with higher strain concentration
262 are more prone to be the source of future earthquakes, thus the relative minimum observed
263 in the L'Aquila basin should not necessarily represent a decrease of the probability of
264 earthquake occurrence, but could be interpreted as due to the locked part of the fault in the
265 brittle upper crust approaching the end of the seismic cycle (Doglioni et al., 2011;
266 Lundgren et al., 2009).

267 Despite the high concentration of the stations in the L'Aquila area, more near field studies
268 are necessary to solve the behaviour of the crust in this region, still keeping open the
269 debate.

270

271 **Acknowledgments**

272 We are thankful to Angelo Massucci and Sergio Del Mese for the CAGeoNet field work
273 and data storage.

274 **References**

275

276 Anderson, H. and J. Jackson (1987). Active tectonics of the Adriatic region, *Geophys. J. R.*
277 *Astron. Soc.* 91, 937-983.

278

279 Anzidei, M., A. Galvani, A. Esposito, P. Cristofolletti, A. Pesci, P. Baldi, G. Casula, N.
280 Cenni, F. Loddo and E. Serpelloni (2003). The Central Apennines Geodetic Network (CA-
281 Geonet): description and preliminary results, XXVIII European Geophysical Society
282 General Assembly, *Geophys. Res.: Abstr.*, vol 5, abstr EAE03-A-05288.

283

284 Anzidei, M., P. Baldi, A. Pesci, A. Esposito, A. Galvani, F. Loddo, P. Cristofolletti, A.
285 Massucci and S. Del Mese (2005). Geodetic deformation across the Central Apennines
286 from GPS data in the time span 1999-2003, *Annals of Geophysics*, 48 (2), 259-271.

287

288 Anzidei, M., P. Baldi and E. Serpelloni (2008). The coseismic ground deformations of the
289 1997 Umbria-Marche earthquakes: a lesson for the development of new GPS networks,
290 *Annals of Geophysics*, 51, 27-43.

291

292 Anzidei, M., E. Boschi, V. Cannelli, R. Devoti, A. Esposito, A. Galvani, D. Melini, G.
293 Pietrantonio, F. Riguzzi, V. Sepe, and E. Serpelloni, (2009). Coseismic deformation of the
294 destructive April 6, 2009 L'Aquila earthquake (central Italy) from GPS data, *Geophys. Res.*
295 *Lett.*, 36, L17307, doi:10.1029/2009GL039145.

296

297 Avallone, A., G. Selvaggi, E. D'Anastasio, N. D'Agostino, G. Pietrantonio, F. Riguzzi, E.
298 Serpelloni, M. Anzidei, G. Casula, G. Cecere, C. D'Ambrosio, P. De Martino, R. Devoti, L.
299 Falco, M. Mattia, M. Rossi, F. Obrizzo, U. Tammara, and L. Zarrilli (2010). The RING
300 network: improvements to a GPS velocity field in the central Mediterranean, *Annals of*
301 *Geophysics*, 53 (2), doi: 10.4401/ag-4549.

302

303 Basili, R. and S. Barba (2007). Migration and shortening rates in the northern apennines,
304 Italy: implications for seismic hazard, *Terra Nova* 19, 462-468, doi: 10.1111/J.1365-
305 3121.2007.00772.x 2007.

306

307 Beutler, G. et al. (2007). Bernese GPS Software, edited by R. Dach, U. Hugentobler, P.
308 Fridez and M. Meindl (Eds), Astronomical Institute, University of Bern (January 2007).

309

310 Boccaletti, M., C. Conedera, P. Dainelli and P. Gocev (1982). The recent (Miocene–
311 Quaternary) tectonic system of the western Mediterranean region, *J. Pet. Geol.*, 5, 31-49.

312

313 Boschi, E., E. Guidoboni, G. Ferrari, and G. Valensise (1998). I terremoti dell'Appennino
314 Umbro-Marchigiano (area sud orientale dal 99 a. C. al 1984), ING-SGA, compositori,
315 Bologna, Italy.

316

317 Calais, E., J.M. Noquet, F. Jouanne, and M. Tardy (2002). Current strain regime in the
318 western Alps from continuous Global Positioning System measurements, 1996-2001,
319 *Geology* 7, 651-654.

320

321 D'Agostino, N., D. Cheloni, S. Mantenuto, G. Selvaggi, A. Michelini, and D. Zuliani
322 (2005). Strain accumulation in the southern Alps (NE Italy) and deformation at the
323 northeastern boundary of Adria observed by CGPS measurements, *Geophys. Res. Lett.* 32,
324 L19306, doi: 10.1029/2005GL024266.

325

326 D'Agostino, N. A. Avallone, D. Cheloni, E. D'Anastasio, S. Mantenuto, and G. Selvaggi,
327 (2008). Active tectonics of the Adriatic region from GPS and earthquake slip vectors, *J.*
328 *Geophys. Res.* 113, B12413, doi: 10.1029/2008JB005860.

329

330 Devoti, R., F. Riguzzi, M. Cuffaro and C. Doglioni (2008). New GPS constraints on the
331 kinematics of the Apennines subduction, *Earth Planet Sci. Lett.* 273, 163-174.

332

333 Devoti, R., A. Esposito, G. Pietrantonio, A.R. Pisani, and F. Riguzzi (2011). Evidence of
334 large scale deformation patterns from GPS data in the Italian subduction boundary, *Earth*
335 *and Planet. Sci. Lett.* 311, 230-241, doi: 10.1016/J.epsl.2011.09.034.

336

337 Devoti, R., E. Flammini, G. Pietrantonio, F. Riguzzi and E. Serpelloni (2012). Toward a
338 dense Italian GPS velocity field: data analysis strategies and quality assessment, N. Sneeuw
339 et al. (eds.), *VII Hotine-Marussi Symposium on Mathematical Geodesy*, International
340 Association of Geodesy Symposia 137, DOI 10.1007/978-3-642-22078-4 51, Springer-
341 Verlag Berlin Heidelberg.
342

343 Doglioni, C. (1991). A proposal for Kinematic modeling of W-dipping subduction-possible
344 applications to the Tyrrhenian-Apennines system, *Terra Nova* 3, 423-434.
345

346 Doglioni, C., F. Mongelli and P. Pieri (1994). The Puglia uplift (SE Italy): an anomaly in
347 the foreland of the Apenninic subduction due to buckling of a thick continental lithosphere,
348 *Tectonics* 13, 1309-1321.
349

350 Doglioni, C., S. Barba, E. Carminati and F. Riguzzi (2011). Role of the brittle-ductile
351 transition on fault activation, *Phys. Earth Planet. Inter.* 184, 160-171, doi:
352 10.1016/j.pepi.2010.11.005.
353

354 Dong, D. and R.W. Bock (1989). GPS network analysis with phase ambiguity resolution
355 applied to crustal deformation studies in California, *J. Geophys. Res.* 94, 3949-3966.
356

357 Faure Walker, J.P., G.P. Roberts, P.R. Sammonds and P. Cowie (2010). Comparison of
358 earthquake strains over 10^2 and 10^4 year timescales: Insights into variability in the seismic
359 cycle in the central Apennines, Italy, *J. Geophys. Res.* 115, B10418, doi:
360 10.1029/2009JB006462
361

362 Frepoli, A. and A. Amato (1997). Contemporaneous extension and compression in the
363 Northern Apennines from earthquake fault-plane solutions, *Geophys. J. Int.*, 129, 268-388.
364

365 Galadini, F. and P. Messina (1994). Plio-Quaternary tectonic of the Fucino basin and
366 surroundings areas (central Italy), *Giorn. Geol.*, 56, 73-99.
367

368 Galadini, F. and P. Galli (2000). Active tectonics in the Central Apennines (Italy) – input
369 data for seismic hazard assessment, *Nat. Hazard*, 22, 225-270.
370

371 Herring, T., R.W. King, and S. McClusky (2006). GAMIT Reference Manual, Release
372 10.3. Department of Earth, Atmospheric, and Planetary Sciences, Massachusetts Institute
373 of Technology. (<http://www-gpsg.mit.edu/~simon/gtgk/>).
374

375 Lundgren, P., Eric A. Hetland, L. Zhen, and Eric J. Fielding (2009). Southern San Andreas-
376 San Jacinto fault system slip rates estimated from earthquake cycle models constrained by
377 GPS and interferometric synthetic aperture radar observation, *J. Geophys. Res.*, 114,
378 B02403, doi:10.1029/2008JB005996.
379

380 Malinverno, A. and W.B.F. Ryan (1986). Extension in the Tyrrhenian sea and shortening in
381 the Apennines as result of arc migration driven by sinking of the lithosphere, *Tectonics* 5,
382 227-245.
383

384 McCarthy, D. D. and G. Petit (2004). IERS Conventions (2003). IERS Technical Note 32,
385 Verlag des Bundesamts für Kartographie und Geodäsie, Frankfurt, paperback, ISBN 3-
386 89888-884-3 (print version).
387

388 McClusky, S., S. Balassanian, A. Barka, C. Demir, S. Ergintav, I. Georgiev, O. Gurkan, M.
389 Hamburger, K. Hurst, H. Kahle, K. Kastens, G. Kekelidze, R. King, V. Kotzev, O. Lenk, S.
390 Mahmoud, A. Mishin, M. Nadariya, A. Ouzounis, D. Paradissis, Y. Peter, M. Prilepin, R.
391 Reilinger, I. Sanli, H. Seeger, A. Tealeb, M.N. Toksöz and G. Veis (2000). Global
392 Positioning system constraints on plate kinematics and dynamics in the eastern
393 Mediterranean and Caucasus, *J. Geophys. Res.*, 105, 5695-5719.
394

395 Noquet, J.M., E. Calais, Z. Altamimi, P. Sillard, and C. Boucher (2001). Intraplate
396 deformation in western Europe deduced from analysis of the International Terrestrial
397 Reference Frame 1997 (ITRF97) velocity field, *J. Geophys. Res.* 106 (B6), 11.239-11.257.
398

399 Patacca, E., R. Sartori and P. Scandone (1990). Tyrrhenian basin and Apenninic arcs;
400 kinematic relations since Late Tortonian times, *Mem. Soc. Geol. It.* 45, 425-451.
401

402 Pesci, A., G. Teza, G. Casula, N. Cenni, and F. Loddo (2010). Non-permanent GPS data for
403 regional-scale kinematics: reliable deformation rate before the 6 April, 2009, earthquake in
404 the L'Aquila area, *Annals of Geophysics*, 53 (2), doi: 10.4401/ag-4740.
405

406 Reutter, K.J., P. Gieseand, and H. Closs (1980). Lithospheric split in the descending plate:
407 observations from the Northern Apennines, *Tectonophysics* 64, T1-T9.
408

409 Royden, L., E. Patacca, and P. Scandone (1987). Segmentation and configuration of
410 subducted lithosphere in Italy: an important control on thrust-belt and foredeep-basin
411 evolution, *Geology* 15, 714-717.
412

413 Schaffrin, B. and Y. Bock, (1988). A unified scheme for processing GPS phase
414 observations, *Bulletin Geodesique* 62, 142-160.
415

416 Selvaggi, G. (1998). Spatial distribution of horizontal seismic strain in the Apennines from
417 historical earthquakes, *Ann. Geof.* 41 (2), 241-251.
418

419 Selvaggi, G., RING Working Group (2006). La Rete Integrata nazionale GPS (RING)
420 dell'INGV: una infrastruttura aperta per la ricerca scientifica, X Conferenza nazionale
421 dell'ASITA Bolzano (Italy), 14-17 novembre.
422

423 Serpelloni, E., M. Anzidei, P. Baldi, G. Casula and A. Galvani (2005). Crustal velocity and
424 strain-rate fields in Italy and surrounding regions: new results from the analysis of
425 permanent and non-permanent GPS networks, *Geophys. J. Int.*, 161(3), 861-880.
426 doi:10.1111/j.1365-246X.2005.02618.x.
427

428 Serpelloni, E., G. Casula, A. Galvani, M. Anzidei, and P. Baldi, (2006). Data analysis of
429 permanent GPS networks in Italy and surrounding regions: application of a distributed

430 processing approach, *Annals of Geophysics*, 49, 897-928.

431

432 Shen, Z-K., D.D. Jackson and B.X. Ge (1996). Crustal deformation across and beyond the
433 Los Angeles basin from geodetic measurements, *J. Geophys. Res.*, 101 (B12), 27957-
434 27980.

435

436 Shen, Z-K., D.D. Jackson and Y.Y. Kagan (2007). Implication of Geodetic Strain Rate for
437 future earthquakes, with a five-year forecast of M5 earthquakes in southern California, *Seis*
438 *Res. Lett.*, 78 (1), 116-120.

439

440 Valensise, G. and D. Pantosti (editors) (2001). Database of potential sources for
441 earthquakes larger than M 5.5 in Italy, *Ann. Geof. suppl.* Vol. 4484.

442

443 Vespe, F., G. Bianco, M. Fermi, C. Ferraro, A. Nardi and C. Sciarretta (2000). The Italian
444 GPS fiducial network: services and products, *J. Geodyn.*, 30, 327-336.

445 **Tables**

station	lat	lon	East mm/yr	sigE mm/yr	North mm/yr	sigN mm/yr	smaj-ax mm	smin-ax mm	azim
ACCU	42.696	13.241	0.5	1.0	3.2	1.7	2.5	1.5	-173
AQUI	42.368	13.350	0.5	0.1	2.9	0.1	0.1	0.1	90
ARAG	42.411	13.459	-0.2	0.6	3.3	1.1	1.7	0.9	-171
ASCO	42.822	13.637	1.7	0.3	2.3	0.3	0.5	0.4	176
ATRA	42.551	14.007	0.8	0.2	2.6	0.3	0.5	0.3	9
BANO	42.337	13.582	0.2	1.1	2.4	1.9	3.0	1.6	-171
BLRA	41.810	13.560	-0.4	0.2	3.3	0.4	0.6	0.3	-168
BORB	42.511	13.162	0.3	1.0	1.5	1.4	2.1	1.4	-179
BSPI	42.306	13.650	1.0	1.3	1.4	2.0	3.0	1.9	-171
BSSO	41.546	14.594	0.8	0.1	3.6	0.2	0.3	0.2	-174
CADO	42.293	13.483	-0.3	0.6	2.3	0.9	1.3	0.9	-176
CAME	43.112	13.124	2.1	0.0	3.6	0.1	0.1	0.1	179
CASB	42.390	12.849	-1.1	0.9	1.7	1.5	2.3	1.4	179
CDRA	42.368	13.720	-0.5	0.2	3.9	0.3	0.5	0.3	-170
CEPP	42.530	12.855	-0.8	0.6	1.2	0.9	1.4	0.9	-169
CERT	41.949	12.982	-1.1	0.2	1.8	0.2	0.4	0.2	-173
CESI	43.005	12.905	0.3	0.3	3.6	0.4	0.6	0.4	-171
CHNO	42.654	13.062	-0.2	1.3	4.4	2.0	3.1	1.9	-174
CINC	42.008	13.405	-0.3	1.4	1.2	2.3	3.5	2.0	-170
CORT	42.827	12.987	2.0	1.3	4.9	2.1	3.2	2.0	-173
CPAG	42.501	13.288	-0.2	0.6	2.8	0.9	1.3	1.0	-166
CROG	42.586	13.485	0.5	0.8	2.1	1.2	1.9	1.3	-177
CTOS	42.564	13.359	1.8	1.1	3.4	1.8	2.7	1.7	-176
CVAL	41.984	13.811	0.0	1.4	3.9	2.4	3.7	2.0	-171
CVSE	42.131	13.745	0.1	1.4	4.1	2.2	3.4	2.1	-173
FCLM	42.111	13.459	-0.4	1.2	2.3	2.0	3.1	1.8	-171
FRCA	42.059	13.678	1.0	1.3	2.2	2.1	3.2	1.9	-172
FRRA	42.418	14.292	0.8	0.2	3.1	0.3	0.5	0.3	-172
INGP	42.383	13.316	0.8	0.1	2.9	0.2	0.3	0.2	-175
INGR	41.828	12.515	-0.7	0.1	1.8	0.1	0.2	0.1	-172
LARI	41.810	14.922	1.5	0.4	4.2	0.4	0.7	0.6	172
LNSS	42.603	13.040	1.1	0.2	2.1	0.3	0.4	0.2	7
MOSE	41.893	12.493	-0.5	0.2	2.0	0.3	0.4	0.3	177
MAON	42.428	11.131	-0.6	0.1	0.8	0.2	0.3	0.2	-175
MICI	42.460	13.054	-0.2	0.9	2.0	1.4	2.1	1.4	-171
MLNN	41.822	13.705	-1.1	1.6	2.6	2.7	4.1	2.4	-169
MMAR	42.102	13.363	-1.2	0.7	2.5	1.2	1.9	1.0	-173
MRPN	41.886	13.685	-1.0	1.7	2.0	2.7	4.2	2.5	-173
MRRA	42.885	13.916	1.4	0.2	3.1	0.3	0.5	0.3	-172
MSAN	42.761	13.154	1.3	0.9	2.9	1.2	1.9	1.3	-170
MSNI	42.527	13.363	1.1	1.0	2.4	1.6	2.5	1.4	-173
OCRA	42.050	13.039	-1.2	0.4	2.1	0.6	0.9	0.5	9
PBRA	42.124	14.229	0.1	0.2	3.8	0.3	0.5	0.3	-171
PERU	43.111	12.394	0.6	0.4	1.9	0.5	0.8	0.6	165
PESC	42.024	13.667	0.1	1.1	2.1	1.7	2.6	1.6	-170
POCA	42.571	13.326	0.7	0.9	4.3	1.2	1.8	1.3	-177
POGB	42.515	12.873	0.3	0.8	1.4	1.3	2.1	1.2	9

PPEZ	42.183	13.426	0.7	1.2	2.5	2.0	3.1	1.7	-175
PSCA	42.128	13.125	-1.2	1.1	2.3	1.8	2.7	1.7	-174
PSMA	42.127	13.581	0.8	1.1	2.1	1.7	2.6	1.7	-175
PSTE	42.428	11.120	-0.1	0.7	1.0	0.8	1.2	1.1	164
REFO	42.956	12.704	0.8	0.1	2.2	0.2	0.2	0.2	-173
RENO	42.793	13.093	1.0	0.1	2.3	0.1	0.2	0.1	-171
REPI	42.952	12.002	-0.1	0.1	2.1	0.2	0.2	0.1	-173
RETO	42.782	12.407	-0.2	0.1	1.8	0.1	0.2	0.1	-173
RIET	42.408	12.857	0.1	0.5	0.0	0.6	1.0	0.8	177
RIFP	42.763	13.176	0.9	0.9	3.6	1.4	2.1	1.4	-174
RNI2	41.703	14.152	0.3	0.1	3.1	0.2	0.4	0.2	7
ROCA	42.328	13.697	0.5	1.0	3.0	1.6	2.5	1.5	-173
ROFA	42.397	13.541	-0.1	0.7	1.3	1.1	1.6	1.0	-174
ROIO	42.327	13.386	0.1	0.4	3.6	0.5	0.8	0.6	176
RSTO	42.658	14.001	1.2	0.0	3.3	0.1	0.1	0.1	-177
S260	42.601	13.257	0.8	1.2	2.8	1.8	2.8	1.8	-170
SCIN	42.434	13.559	0.0	0.6	3.4	1.1	1.7	0.9	-171
SCRA	42.268	14.002	0.3	0.2	3.0	0.3	0.4	0.3	-171
SECI	42.148	13.670	0.9	1.2	4.2	1.8	2.8	1.8	-174
SELL	42.369	13.180	1.1	0.7	3.1	0.9	1.3	1.0	176
SI01	42.964	11.901	-0.2	0.6	2.2	0.7	1.1	0.9	173
SIER	41.925	13.668	-0.1	1.1	1.9	1.9	2.8	1.7	-173
SLLI	42.727	13.121	0.6	1.6	3.0	2.4	3.6	2.3	-174
SLUC	42.567	13.261	1.0	1.5	3.9	2.1	3.3	2.2	5
SMCO	42.393	13.271	-0.3	0.6	3.7	0.9	1.4	0.9	-179
SMPQ	42.055	13.394	0.3	0.8	2.0	1.4	2.1	1.2	-173
SMRA	42.048	13.924	0.7	0.2	3.0	0.3	0.4	0.3	-170
SORB	42.082	13.317	-0.6	1.2	2.2	1.9	2.9	1.8	-174
SS83	41.842	13.780	-0.4	1.7	2.0	2.8	4.2	2.5	-173
SSMF	42.131	13.221	0.2	1.0	1.7	1.6	2.5	1.6	-177
SSTS	42.360	13.651	0.8	1.1	1.8	2.1	3.1	1.7	-172
TARI	42.459	13.276	0.8	1.2	2.0	1.9	2.9	1.8	-170
TNER	42.237	13.532	-0.5	1.1	1.2	2.0	3.0	1.7	-173
TODI	42.781	12.408	-0.6	0.6	2.2	0.7	1.1	0.9	155
TOLF	42.064	12.000	-0.9	0.1	1.8	0.2	0.3	0.2	-174
TRAS	41.954	13.543	0.1	1.1	3.2	1.6	2.5	1.6	11
TRIV	41.767	14.550	0.7	0.2	3.6	0.3	0.5	0.3	-171
TRMT	42.096	13.201	-1.2	0.7	2.8	1.2	1.9	1.0	-172
TRNE	42.441	13.198	0.7	0.8	2.7	1.3	2.0	1.2	-173
UNOV	42.716	12.113	-0.1	0.2	1.7	0.3	0.5	0.3	-172
UNPG	43.119	12.356	-0.4	0.1	1.9	0.2	0.2	0.2	179
UNTR	42.559	12.674	0.7	0.1	1.7	0.2	0.2	0.2	179
VCRA	42.735	13.498	1.3	0.2	3.0	0.4	0.6	0.3	-174
VITE	42.418	12.119	-0.9	0.7	1.9	0.8	1.2	1.0	177
VNRE	42.001	13.646	0.5	0.9	1.9	1.6	2.4	1.4	-173
VRCE	42.039	13.240	0.1	0.8	2.5	1.3	2.0	1.1	-174
VTRA	42.110	14.708	0.5	0.2	2.9	0.3	0.4	0.3	-171
VVLO	41.870	13.623	-0.2	0.1	2.6	0.2	0.3	0.2	-174

446

447 **Table 1**

448 **Figure caption**

449 **Fig. 1:** Geological settings of the Umbria-Marche Apennines (UMA) Lazio-Abruzzo
450 Apennines (LAA): main fault systems and intramontane basins, Terni basin (TB), Rieti
451 basin (RB), L'Aquila basin (AB), Fucino basin (FB), Sulmona basin (SB) are reported with
452 instrumental (1978-2008) and historical ($I>10$) (CPTI04)
453 (<http://emidius.mi.ingv.it/CPTI04>) seismicity distribution.

454 **Fig. 2 :** The CAGeoNet (triangles) and the CGPS stations (blue dots) used in our analyses.

455 **Fig. 3:** The residuals between the combined and the individual (BERNESE, GAMIT)
456 solutions.

457 **Fig. 4:** GPS combined velocity field estimated for the time span 1999-2007 with respect to
458 the Eurasian plate. CAGeoNet GPS velocities are shown with red arrows; continuous GPS
459 velocities are shown with blue arrows.

460 **Fig. 5:** The velocity projection along the transect directions 1a–1b / 2a–2b. The projection
461 involved vertices at a distance of 20 and 15 km in both perpendicular directions along the
462 transect directions for the profile 1a -1b and 2a – 2b respectively.

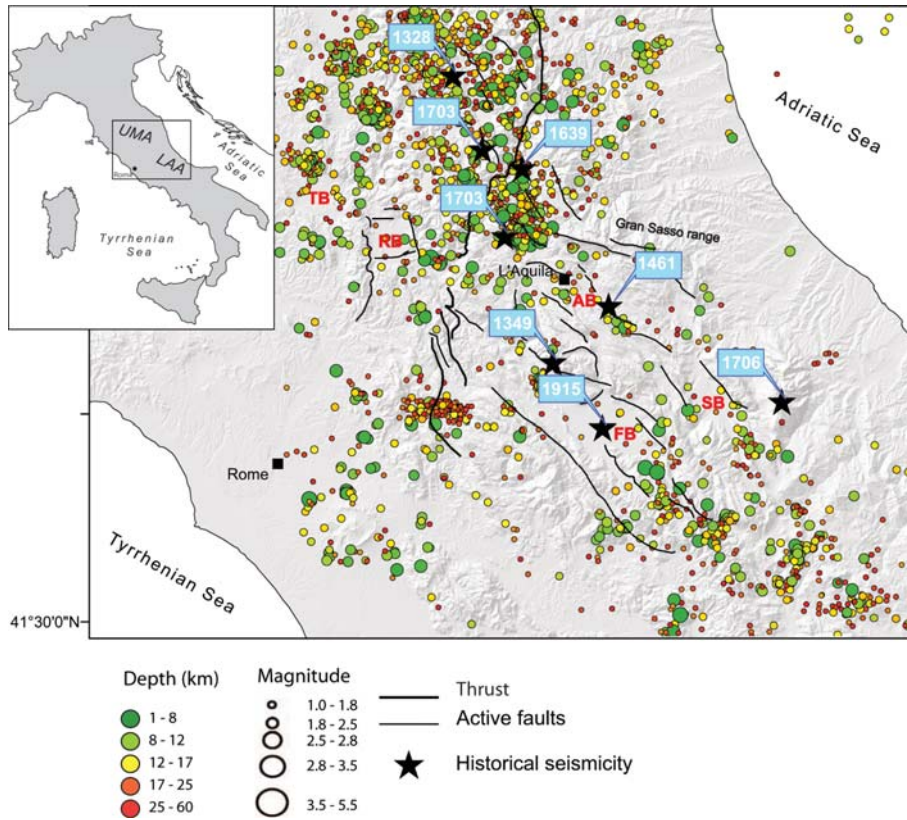
463 **Fig. 6:** The second invariant estimated on a $0.1^\circ \times 0.1^\circ$ regular grid according to the
464 algorithm of Shen et al. (1996).

465

466 **Table caption**

467 Table1. Velocity field (mm yr^{-1}) of the CAGeoNet and of the surrounding CGPS stations
468 used in the analysis. In the columns are reported site name, site coordinates, velocities E
469 and N (both in mm yr^{-1}), sigma E and sigma N (both in mm yr^{-1}) and error ellipses with
470 azimuth.

471

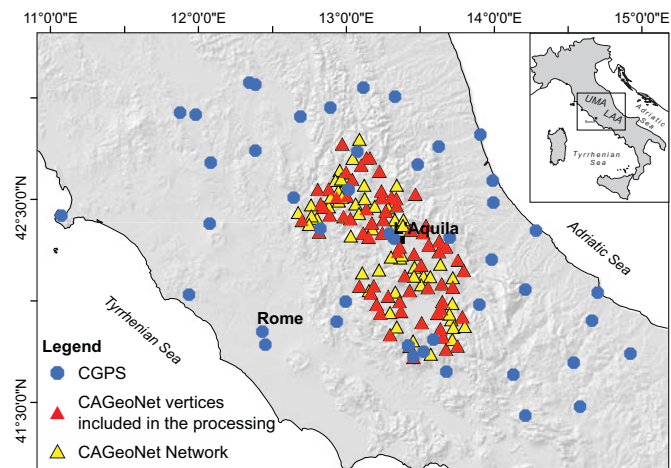


472

473

474 **Figure 1**

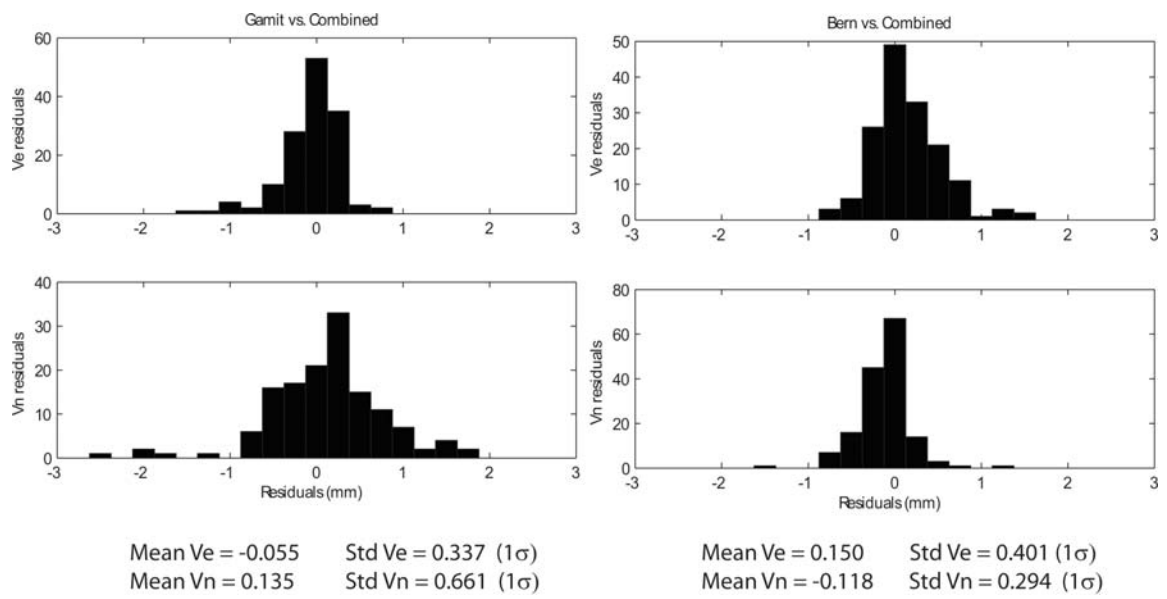
475



476

477

478 **Figure 2**

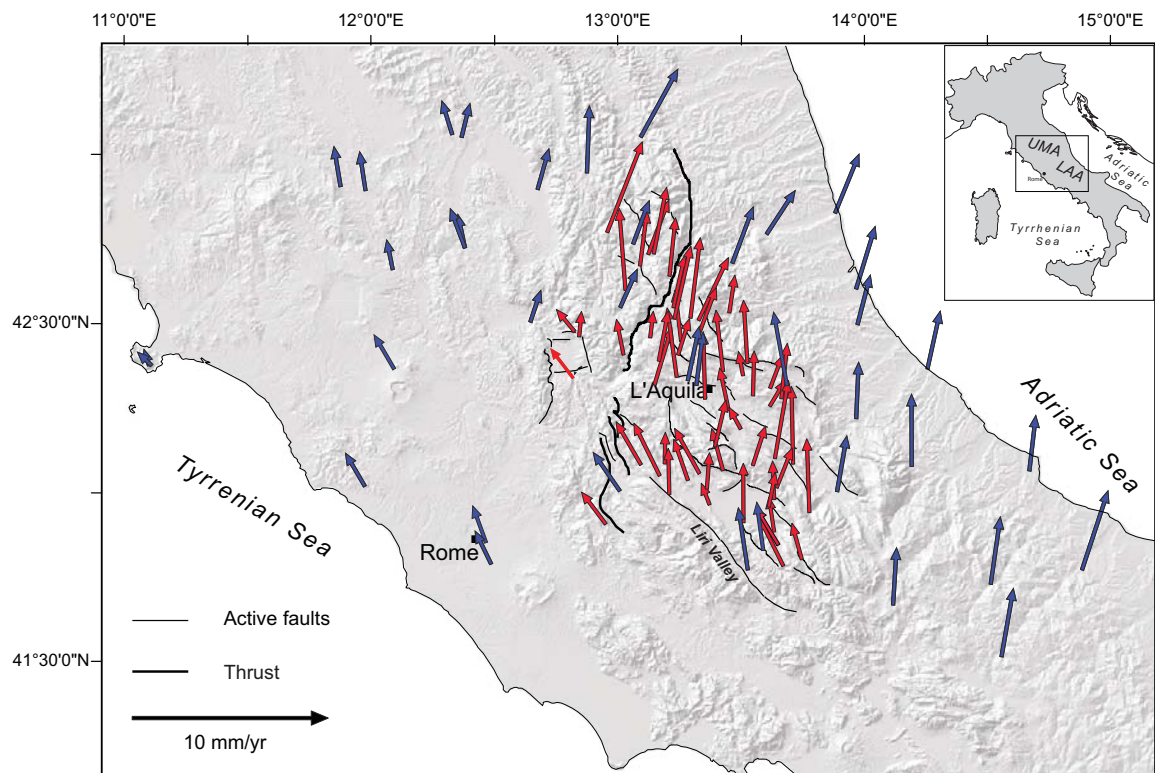


479

480

481 **Figure 3**

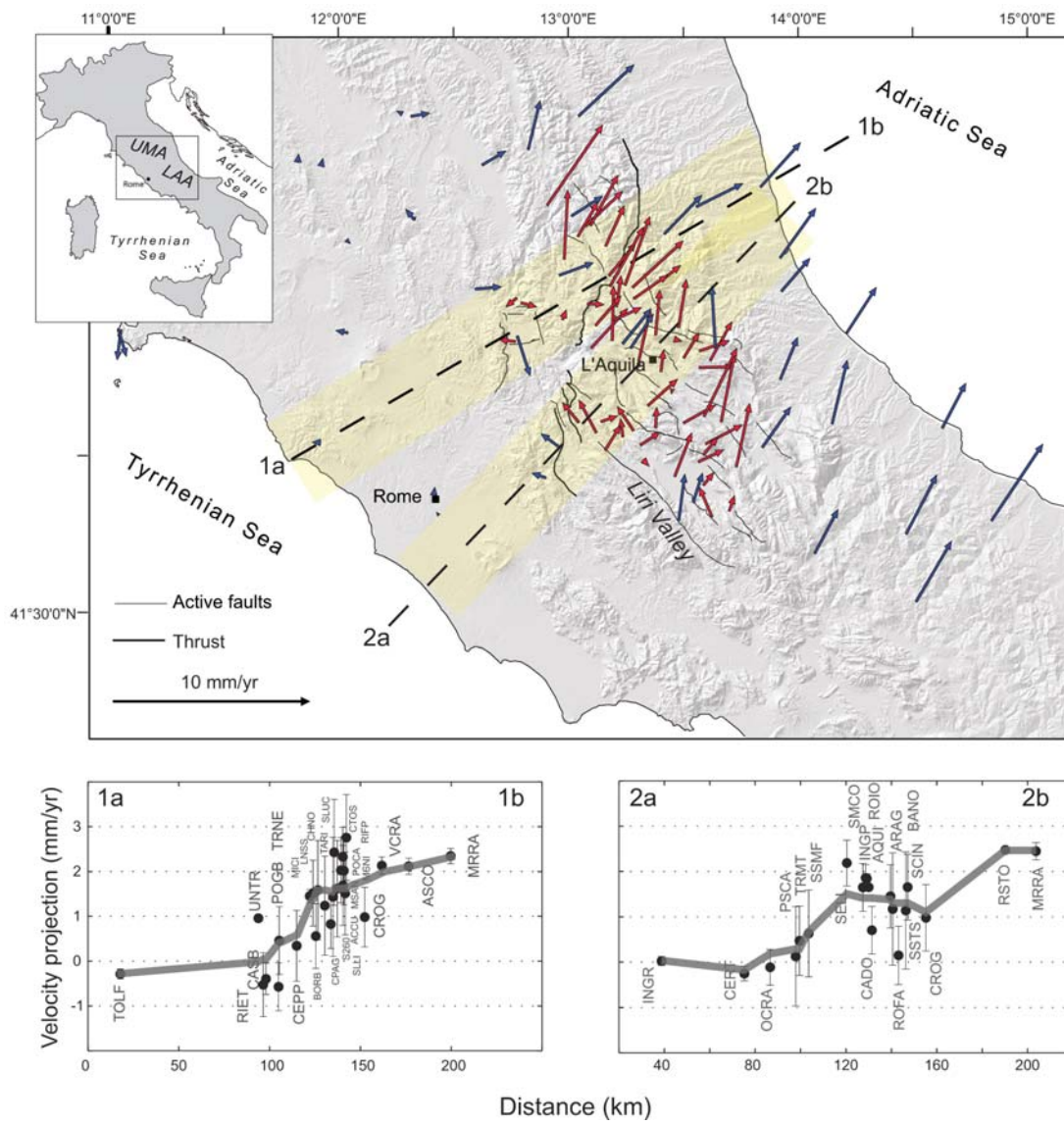
482



483

484 **Figure 4**

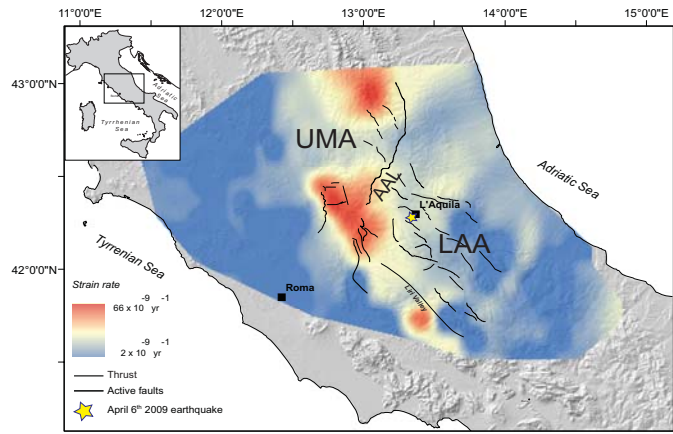
485



486

487 **Figure 5**

488



489

490

491 **Figure 6**